The sensitivity of shaped pupil coronagraphs to optical aberrations

Joseph J. Green[†] and Stuart B. Shaklan
Jet Propulsion Laboratory, California Institute of Technology

Robert J. Vanderbei and N. Jeremy Kasdin
Princeton University

ABSTRACT

Unlike focal-plane coronagraphs that use occulting spots and Lyot stops to eliminate diffraction, pupil-plane coronagraphs operate by shaping the pupil to redirect the diffracted stellar light into a tight core. As in focal-plane coronagraphs, the optical aberrations in the telescope must be sufficiently corrected to enable high contrast imaging. However, in shaped-pupil coronagraphs, the low-order aberrations resulting from misalignment and optical figure drift have a much smaller influence upon the contrast at the inner working angle. These weaker sensitivities greatly relax the strict low-order wavefront stability required for high-contrast imaging at the cost of some throughput. In this paper, we present the simulated performance of the concentric ring shaped pupil concepts comparing them to focal-plane coronagraphs that are optimized for the same inner working angles.

Keywords: shaped pupil, coronagraphic telescope, error modeling, optical aberrations, extrasolar planets

1. INTRODUCTION

NASA is planning to launch the Terrestrial Planet Finder (TPF) Coronagraph, a visible to near-infrared large-aperture coronagraphic telescope, in the middle of the next decade. The baseline TPF design is a monolithic 6x3.5 meter off-axis Cassegrain optical telescope with a high-density, low-bandwidth wavefront control system that feeds a coronagraph capable of achieving better than 10^{-10} rejection of starlight. This enables direct detection of starlight reflected from terrestrial planets orbiting some 35 target stars. Already, the TPF High Contrast Imaging Testbed (HCIT) has achieved 10^{-9} contrast in the so-called 'dark hole' region extending from 4-10 Airy rings[1]. The TPF program has been described by Ford et al[2]. General information about the program, technology, and science can be found at http://planetquest.jpl.nasa.gov.

The HCIT has achieved its 10^{-9} contrast result using a band-limited image-plane coronagraph mask[3] partnered with a hard-edged Lyot Stop. The mask, with amplitude transmission approximating $1\text{-sinc}^2(x)$, diffracts light into a finite region outside the Lyot stop. The performance is limited, at least in part, by sub-nm residuals in the corrected wave front. The residuals include uncorrected tilt, focus and astigmatism that result in a uniform illumination of the Lyot Stop, leading to the formation of an ideal (but unwanted!) Airy pattern at the center of the image plane. Coma forms a quadratic illumination. The resulting point spread functions ring with $1/r^3$ intensity decay and are still significant at the inner working angle (IWA), even for minute aberration levels. Green and Shaklan reported on optimizing image-plane coronagraphs to minimize their aberrations sensitivity to such low-order aberrations[4].

The last several years have witnessed the development of an alternative coronagraphs known as shaped-pupil coronagraphs, originally conceived by Spergel[5]. The pupil shapes are binary approximations to continuous apodization functions. Kasdin et al describe the optimization of several apodization and pupil shaping functions[6,7]. Vanderbei et al

[†]Contact information: 4800 Oak Grove Dr., M/S 306-336, Pasadena CA 91109, E-mail: Joseph.J.Green@jpl.nasa.gov

describe several variations of the shaped pupil, including circularly symmetric[8], so-called 'spiderweb' (self-supporting) designs[9], star-shaped[10], and 1-D and rectangular versions[11].

Shaped pupil coronagraphs are designed to share a common characteristic: a very sharp central core with a significant fraction (up to unity, depending on design) of the surrounding region is suppressed to $< 10^{-10}$ of the core peak value. All have the same characteristic insensitivity to low-order aberrations (when compared to image plane masks) to varying degrees. In the following section we describe the selected masks along with the method we employed to optimally represent them within reasonably sampled pupil. In Sect 3 we describe how these pupil representations are used to model the aberrations sensitivity of the concentric ring masks and presents the derived sensitivity models for an elliptical system suitable for TPF. In Sect 4 we compare these aberrations sensitivities to those resulting from a band-limited image-plane coronagraph that has been optimized for the same optical system. We show that the concentric ring masks provide at least an order of magnitude, and in some cases several orders of magnitude, improvement in the aberration sensitivity over image plane coronagraphs.

2. OPTIMIAL DISCRETE REPRESENTATIONS FOR SHAPED PUPIL CORONAGRAPHS

Shaped pupil coronagraphs that enable high contrast imaging over a large working region tend to be comprised of multiple openings that include very small masks features. These small features have been optimized to suppress the diffraction rings caused by the larger openings. In the concentric ring masks, for instance, the thin outer rings carry only a small fraction of the net pupil area but accomplish the last few orders of diffraction suppression. The general form for the concentric ring masks can be written as

$$p(u,v) = \sum_{n=1}^{N} \frac{(-1)^n}{|\rho_n|^2} cyl\left(\frac{1}{\rho_n}\sqrt{(u)^2 + (v/\varepsilon)^2}\right), \tag{1}$$

where $\{\rho_n\}$ represents the set of ring edge radii and ε specifies the pupil ellipticity. To successfully model these binary masks using a discrete binary representation of the pupil one would have to consider prohibitively large array sizes. Fortunately, it has been shown that optimal, discrete and *non-binary* representations of otherwise discrete pupils can be constructed from analytic expressions of their far-field patterns[12]. By taking the Fourier transform of an analytic expression of the far-field pattern evaluated over the field points of interest, a bandlimited representation of the pupil may be constructed. Once created, this pupil may be used to accurately describe the amplitude portion of the imaging system exit-pupil.

In the case of the concentric ring mask, we can write the analytic far-field pattern as,

$$f(x,y) = \sum_{n=1}^{N} \frac{(-1)^n}{2\sqrt{(x)^2 + (\varepsilon y)^2}} J_1\left(\pi\rho_n\sqrt{(x)^2 + (\varepsilon y)^2}\right), \tag{2}$$

and evaluate it over the field at the desired field sampling. To avoid edge effects, we first apply a windowing function to the far-field pattern before taking the Fourier transform. This windowing function is designed to leave the central 200 λ/D intact and then tapers the field amplitude to zero following the Blackman function[13]. Thus, the optimal discrete representation for exit-pupil amplitude is computed as

$$a(u,v) \cong \mathbb{F}\{f(x,y) \times w(x,y)\}, \tag{3}$$

where $\mathbb{F}\{\ \}$ is the Fourier transform and $w(x,y)$ is the window function. Figure 1 shows the discrete, band-limited representations of the IWA = 3.5 λ/D and 4 λ/D concentric-ring masks resulting from this procedure. These masks have been stretched to match the support of an 8x3.5 pupil. Such aperture shapes are currently under considerations for enabling a more extensive TPF mission. Figure 2 shows simulations of the monochromatic and broadband point-spread functions (PSF) resulting from these discrete representations of the pupils. In Figure 3, we show a horizontal slice through the optical axis to illustrate the impact of the optical bandwidth to the inner and outer working angles as well as to the contrast floor.

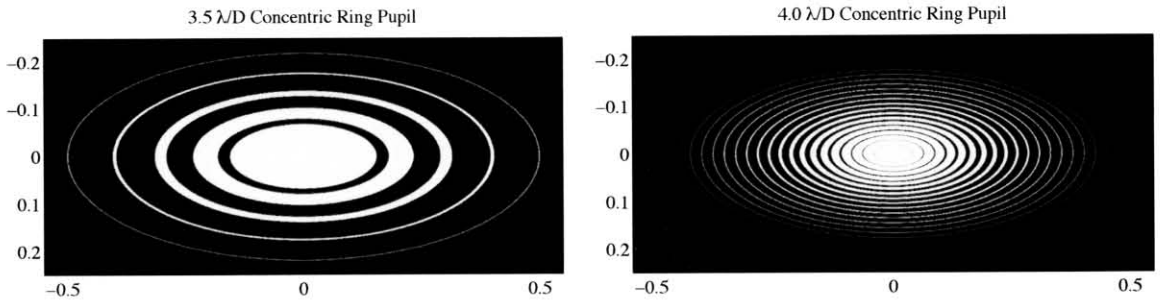

Figure 1: Optimal discrete representations of the 3.5 λ/D (left) and 4.0 λ//D (right) concentring ring masks used in the sensitivity study. These masks have been stretched from the oringialy circullarly symmetric design to match the support of a 8x3.5 elliptical pupil.

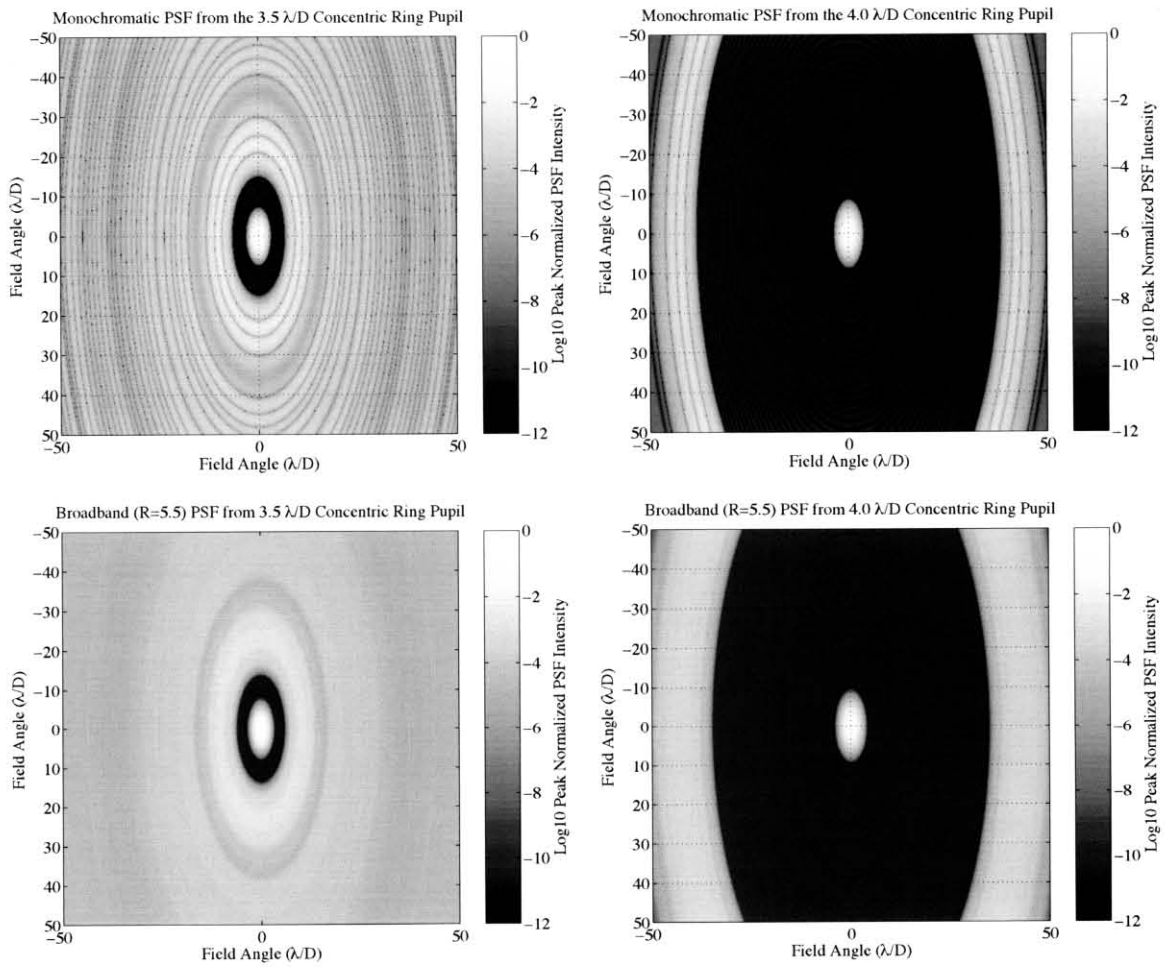

Figure 2: Peak normalized monochromatic PSF calculated for the 3.5 λ/D (top-left) and 4.0 λ/D masks. The bottom rows shows the PSFs computed from the same masks but over a λ/Δλ=5.5 passband.

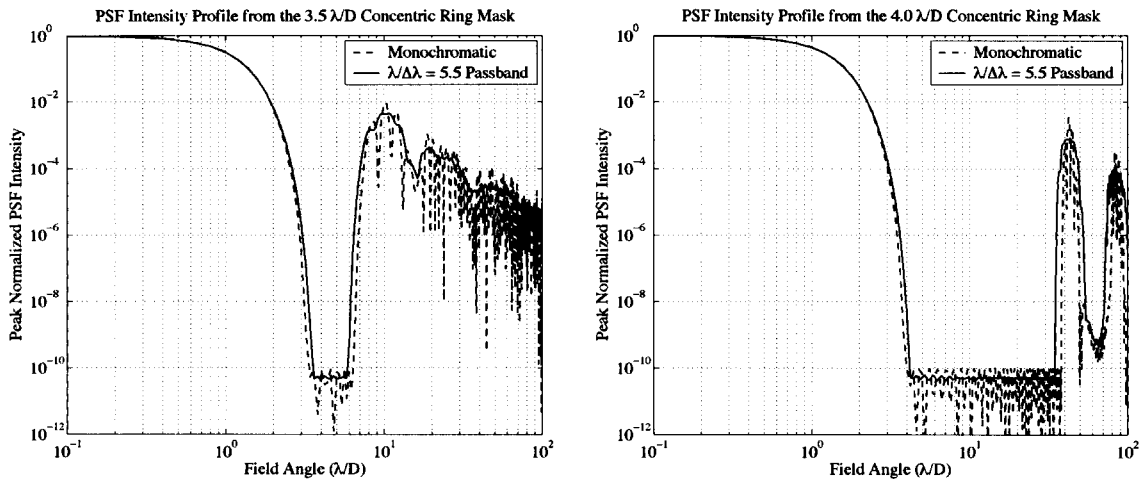

Figure 3: Intensity profiles through the monochromatic and broadband shaped-pupil PSFs depicting the level of diffraction suppression achieved in their designs. The monochromatic PSF is defined at 550nm while the broadband PSF represents a 500-600nm passband that has been composed of 11 monochromatic calculations.

3. LOW-ORDER ABERRATION SENSITIVITY OF THE CONCENTRIC-RING MASKS

Using our pupil representation we can now explore the sensitivity of PSF contrast to low order aberrations. The aberrated exit-pupil of the optical system may be described at a particular wavelength, λ, as

$$p(u,v) = a(u,v)e^{i\frac{2\pi}{\lambda}\theta(u,v)}, \tag{4}$$

where $\theta(u,v)$ is the optical path difference across the exit-pupil[14]. While certainly the proper correction of the wavefront must be achieved to enable high contrast imaging, achieving *stability* of that wavefront may be a much more daunting task. For example, small motions of the secondary mirror induce low-order errors that in turn can quickly degrade contrast. In our earlier work, we showed that Lyot coronagraphs are very sensitive to low-order aberration and thus possess severe telescope stability tolerances[4]. In this section, we now explore such sensitivities for concentric ring masks.

Because we are studying an unobscured 8x3.5 elliptical aperture, we consider the elliptical low-order aberrations that are likely to evolve from system perturbations. In Figure 4 we show the Noll ordered Zernike polynomials used in our study. The Zernikes are stretched in the v axis by ε (see eq. 1) to match the pupil ellipticity. Thus, Zernike mode 4, focus, has curvature c on the u axis and εc on the v axis. To examine the impact of a particular aberration, we simply insert a scaled version of the aberration into eq. (4) and compute the PSF over the optical passband. Figure 5 depicts the impacts of the focus aberration upon the two concentric ring masks contrast evaluated at 4.6 λ/D.

For a particular field angle within the working regions of the masks, the normalized PSF intensity remains unaffected by very weak focus aberration. As the aberration level increases, the floor begins to rise and the PSF core begins to move outwards. At the outer working angle, the boundary where the diffraction suppression suspends moves inward. In the case of the 4 λ/D concentric ring mask, even a large focus error (e.g. lambda/26 waves rms) does not effect the PSF much beyond the inner working angle. Because the 3.5 λ/D concentric ring mask has such a confined working region (where the diffraction suppression > 10^{-10}), a strong focus error fills in the entire suppressed region. The behavior of these PSFs in the presence of is noteworthy for two reasons. First, the amount of focus aberration needed to cause a particular increase in contrast is much higher than we have seen in Lyot coronagraphs[4]. And secondly, the energy from the aberration is well confined to the core. Looking at Lyot coronagraphs, the presence of such optical errors would cause contrast to degrade *everywhere* over the coronagraph field with $1/r^3$ radial decay.

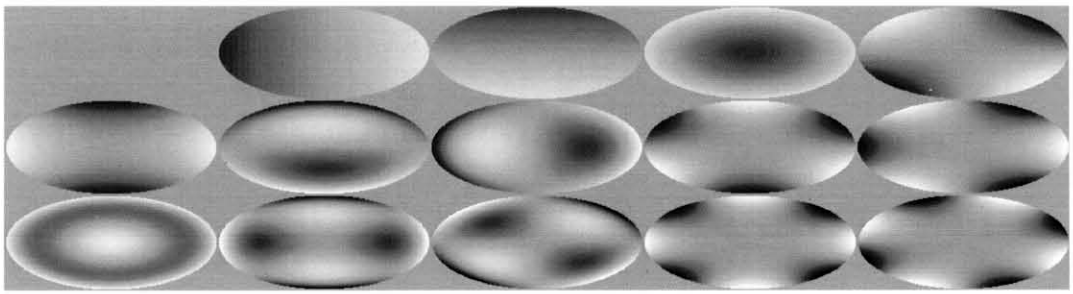

Figure 4: Elliptical Zernike polynomials following the Noll ordering are shown. The top row shows modes 2 though 5 (from left to right). The middle rows shows modes 6-10 and the bottom row shows modes 11-15.

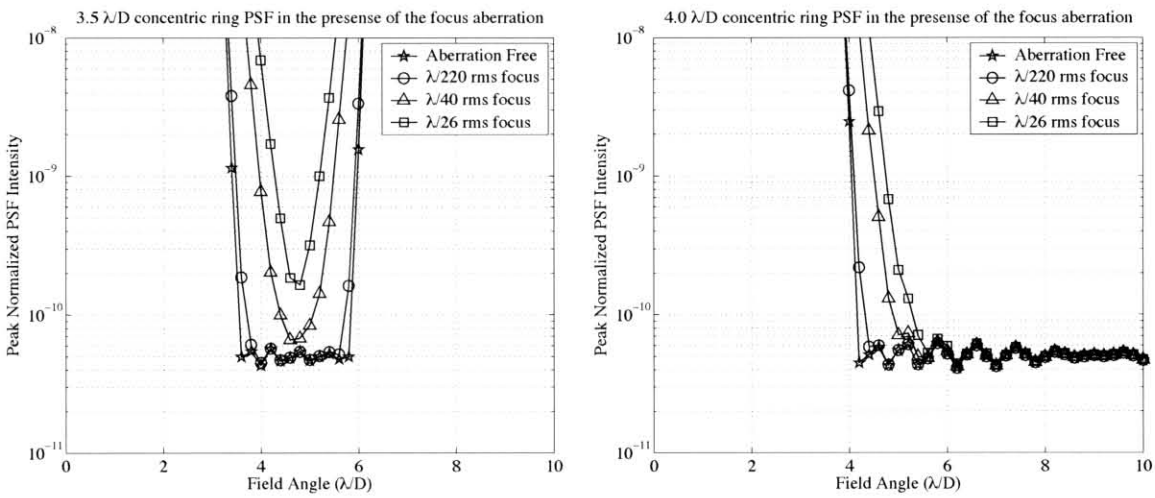

Figure 5: Impact of focus aberrations upon the concentric ring mask PSFs. Because diffraction is shaped by these coronagraphs rather than eliminated, the focus error has little impact upon the light distribution that is well confined to the PSF core.

In Figure 6, we show the change in contrast as function of the rms wavefront error for the elliptical focus, astigmatism and spherical aberrations. At low levels of aberrations, the contrast sensitivity tends to obey a 2nd order power law. As the magnitude of the error increases, however, the order of the sensitivity increases dramatically. This reflects the additional contrast increase caused by the PSF core moving outward. Because we are interested in ultimately establishing telescope stability requirements, we fit a power law to these curves of the form

$$C = 10^{\alpha}\left(\frac{\sigma_m}{\lambda}\right)^{p}, \tag{6}$$

with parameters α and p are being established about a particular contrast level. Tables 1 and 2 list these coefficients for the two concentric ring masks under study over the low-order modes and at several field angles. Because the contrast requirements for observing extrasolar terrestrial planets are so demanding, we fit the parameters for sensitivity models about the contrast level of 10^{-12}.

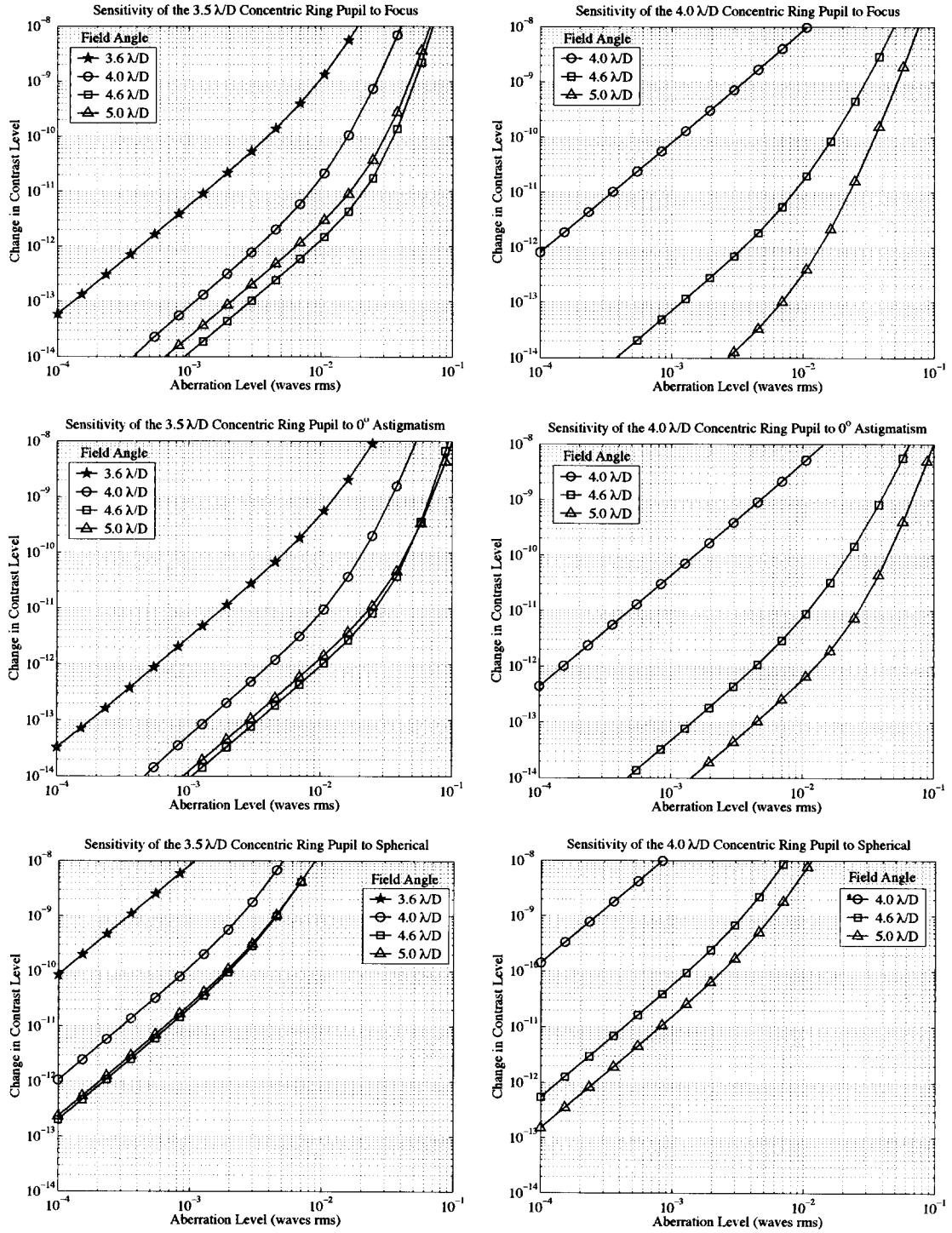

Figure 6: The increase in contrast as a function of focus (top-row), astigmatism (middle-row) and spherical aberration (bottom-row) for the 3.5 λ/D (left column) and 4.0 λ/D (right column) concentric ring masks. The set of curves in each plot depict the evaluation of the contrast change at a particular field angle.

Table 1: Aberration sensitivity models for the 3.5 λ /D concentric ring pupil over a range of field angles

Zernike Mode	3.6 λ/D		4.0 λ/D		4.6 λ/D		5.0 λ/D	
(Noll Ordering)	p	α	p	α	p	α	p	α
2	---	---	---	---	---	---	---	---
3	---	---	---	---	---	---	---	---
4	1.99	-5.29	2.18	-6.59	2.14	-7.62	2.16	-7.27
5	1.95	-6.98	1.72	-8.55	2.26	-8.35	3.15	-7.13
6	1.99	-5.55	2.21	-6.75	2.16	-7.70	2.07	-7.77
7	2.45	-5.02	1.95	-6.71	2.61	-6.33	2.14	-7.09
8	2.00	-3.28	2.01	-4.74	2.07	-5.62	2.01	-5.57
9	2.68	-4.32	1.98	-6.44	1.65	-8.22	5.76	-0.57
10	2.00	-4.18	2.01	-5.56	2.09	-6.45	2.00	-6.46
11	2.00	-2.07	2.01	-3.95	2.01	-4.66	2.01	-4.61
12	2.00	-2.07	2.01	-3.93	2.01	-4.64	2.00	-4.65
13	3.11	-1.73	1.60	-6.86	1.65	-7.31	2.23	-5.38
14	2.00	-3.13	2.01	-4.91	2.00	-5.56	2.01	-5.69
15	2.68	-3.55	1.66	-6.96	1.96	-6.20	1.53	-8.01

Table 2: Aberration sensitivity models for the 4.0 λ /D concentric ring pupil over a range of field angles

Zernike Mode	3.6 λ/D		4.0 λ/D		4.6 λ/D		5.0 λ/D	
(Noll Ordering)	p	α	p	α	p	α	p	α
2	---	---	---	---	---	---	---	---
3	---	---	---	---	---	---	---	---
4	---	---	2.00	-4.10	2.22	-6.54	3.57	-5.31
5	---	---	2.00	-5.54	1.88	-8.24	4.80	-5.96
6	---	---	2.00	-4.37	2.23	-6.72	2.37	-7.49
7	---	---	2.00	-4.82	1.98	-6.66	2.00	-7.51
8	---	---	2.00	-2.58	2.01	-5.06	2.08	-6.00
9	---	---	2.00	-4.90	1.98	-6.52	1.97	-7.26
10	---	---	2.00	-3.49	2.01	-5.88	2.09	-6.74
11	---	---	2.00	-1.85	2.00	-4.25	2.00	-4.81
12	---	---	2.00	-1.86	2.00	-4.24	2.00	-4.78
13	---	---	2.00	-4.03	2.05	-5.37	1.98	-5.98
14	---	---	2.00	-2.97	2.00	-5.27	2.00	-5.71
15	---	---	2.00	-4.94	2.13	-5.83	1.98	-6.29

4. LOW-ORDER ABERRATION SENSITIVITY OF THE RADIAL SINC^2 LYOT CORONAGAPH

For comparison, we created a Lyot coronagraph for the 8x3.5 meter elliptical system. It has an occulting spot with a field transmission of the form

$$occ(x,y) = 1 - \mathrm{sinc}^2\left(\frac{1}{\sigma}\sqrt{x^2 + (\varepsilon y)^2}\right). \tag{7}$$

where σ was chosen to be 5.5 λ/D which provides the optimum coronagraph efficiency at a working angle of 4 λ/D. The occulter is stretched to match the ellipticity of the PSF resulting from the system aperture. The resulting Lyot stop is elliptical and has a net throughput of 38%.

As with the concentric ring masks, we introduced varying amounts of low-order aberrations to explore the sensitivity of this coronagraph. In figure 7, we compare the contrast sensitivities for this Lyot coronagraph to the 3.5 λ/D and 4 λ/D concentric ring masks. In these cases, the Lyot coronagraph has a much higher sensitivity. Looking at the focus error, there is more the four orders of magnitude of additional contrast increase for the same aberration level! The contrast sensitivity models derived from such curves are shown in Table 3. As in our earlier work, we find that Lyot coronagraphs with radial band-limited occulters have some low-order sensitivities that obey a 4th order model instead of a second order model[4].

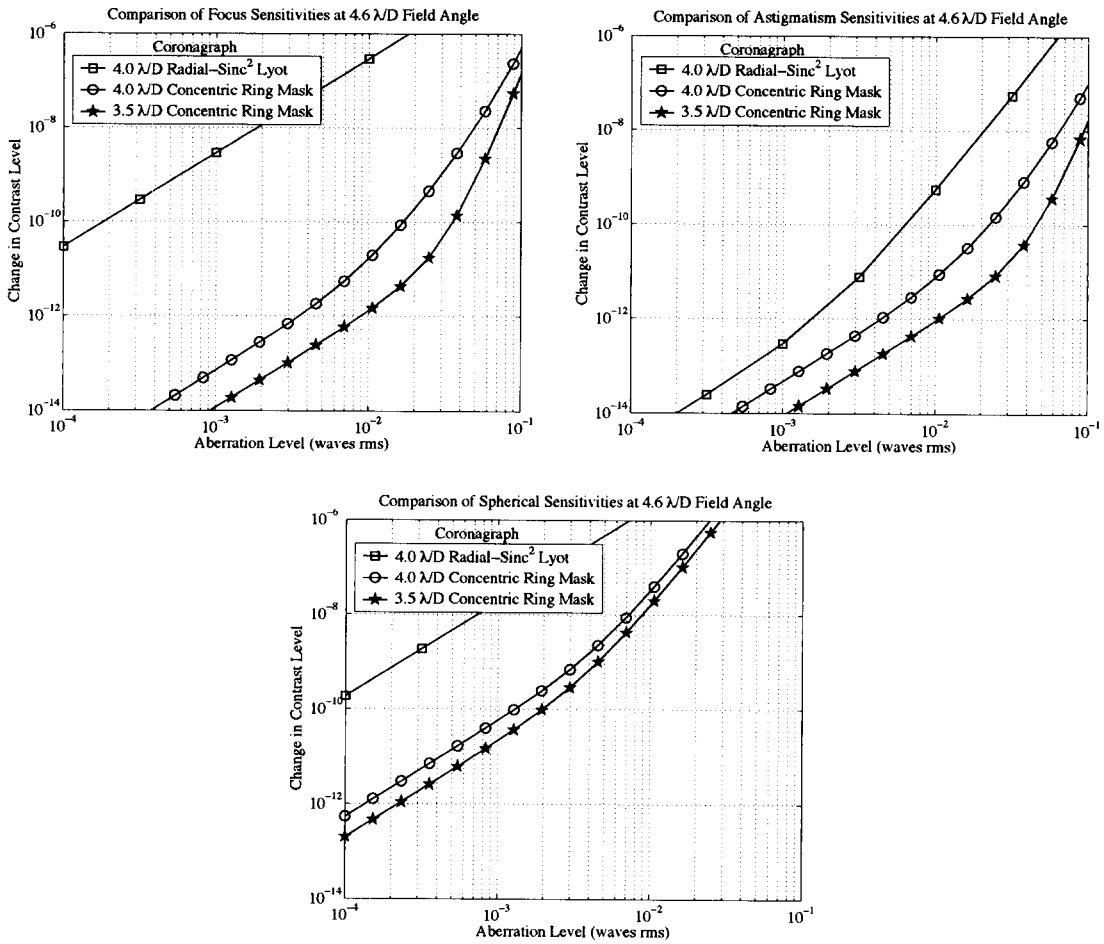

Figure 7: Comparison of the 4.6 λ/D contrast sensitivity to the focus (top-left), astigmatism (top-right) and spherical (bottom) aberrations.

Table 3: Aberration sensitivity models for the 4.0 λ/D radial-sinc^2 Lyot coronagraph a range of field angles

Zernike Mode	3.6 λ/D		4.0 λ/D		4.6 λ/D		5.0 λ/D	
(Noll Ordering)	p	α	p	α	p	α	p	α
2	4.01	-1.62	4.03	-1.84	4.08	-1.92	4.18	-1.91
3	3.99	-1.63	4.02	-1.84	4.08	-1.89	4.17	-1.90
4	2.00	-2.14	2.00	-2.40	2.00	-2.53	2.00	-2.70
5	3.94	-1.04	3.97	-1.15	3.96	-1.33	3.97	-1.52
6	4.11	-0.73	4.11	-0.89	4.08	-1.12	4.06	-1.35
7	2.01	-2.68	2.01	-3.07	2.02	-3.86	2.02	-4.16
8	2.00	-1.06	2.00	-1.31	2.00	-1.68	2.00	-1.73
9	3.95	-0.90	3.97	-0.94	4.00	-1.09	4.02	-1.26
10	3.97	-0.80	4.00	-0.85	4.06	-0.95	4.04	-1.15
11	2.02	-1.35	2.01	-1.45	2.01	-1.71	2.01	-1.95
12	2.01	-0.92	2.01	-1.00	2.00	-1.22	2.00	-1.47
13	2.06	-2.08	2.02	-2.25	2.01	-2.66	2.02	-3.01
14	3.90	-0.94	3.86	-1.07	3.86	-1.28	3.93	-1.35
15	3.98	-0.90	3.97	-0.99	3.97	-1.21	3.95	-1.42

A comparison of the aberration sensitivities is best illustrated by an example set of error allocations as shown in Table 4. This table contains the aberrations tolerances for the Zernike modes such that each one contributes 10^{-12} to the contrast floor. The numbers listed in the table are in rms wavefront in Angstroms and are derived from contrast sensitivity models shown in Tables 1-3. Generally, the concentric ring mask coronagraphs are substantially more tolerant of low-order aberrations than the Lyot coronagraph. The exceptions are some of the modes that possess a 4th order contrast sensitivity in the radial-sinc^2 Lyot coronagraph. In particular trefoil (modes 9 and 10) and quadrafoil (modes 14 and 15) are 2x-4x more tolerable by the radial-sinc^2 Lyot coronagraph than by the concentric ring masks. Note, however, that these tend not drive system stability requirements. The critical modes such as focus (mode 4), astigmatism (modes 5 and 6) and coma (modes 7 and 8) are made much more tolerable with the concentric ring masks. Most noteworthy is the focus aberration tolerance that is relaxed by factors of 200-500 to 1.

Table 4: The values in the table represent the rms wavefront error in Angstroms for a particular Zernike mode to induce a 10^{-12} contrast floor increase at 4.6 λ/D within a 18% optical passband centered at λ =5500Å.

Zernike Mode	4	5	6	7	8	9	10	11	12	13	14	15
3.5 λ/D Concentric Ring Mask	48.76	133.44	56.74	37.20	4.54	28.34	12.07	1.23	1.21	7.92	3.34	6.04
4.0 λ/D Concentric Ring Mask	19.19	55.57	23.84	11.07	1.93	9.26	4.91	0.75	0.73	3.26	2.39	6.93
4.0 λ/D Radial-Sinc^2 Lyot	0.10	11.09	11.76	0.51	0.04	10.30	10.37	0.04	0.02	0.12	9.24	10.56

As a last form of comparison, we examine the efficiency that the planet light is transmitted through each of the coronagraph concepts. Table 5 presents the statistics of encircled energy of the planet PSF for a full-width half-max (radius out to 50% PSF peak intensity) and for a full-width full-max (98% PSF peak intensity). Also listed in the table is the size of the airy core captured within the enclosed region as well as the coronagraphic pupil stop efficiencies. The net airy throughput at the bottom of the table is the product of planet PSF encircled energy with the pupil stop efficiency. The radial-sinc^2 Lyot coronagraph admits about 2-3 times more planet light to the planet PSF core within the same integration time. Its higher aberration sensitivity, however, requires that the telescope alignment remain 10-100 times more stable that what the concentric ring masks would demand.

Table 5: Comparison of the PSF properties and efficiency of the coronagraphs under study

Coronagraph	3.5 λ/D Concentric Ring Mask		4.0 λ/D Concentric Ring Mask		4.0 λ/D Radial-Sinc^2 Lyot	
Enclosing Region (% PSF Peak)	50%	98%	50%	98%	50%	98%
Airy Core Area within Region (λ/D)^2	4.1	22.8	6.0	31.6	5.1	20.8
Planet PSF Encircled Energy	29.0%	57.2%	30.0%	57.2%	48.6%	83.5%
Pupil Mask / Lyot Stop Efficiency	27.0%		18.2%		38.0%	
Net Airy Throughput	7.8%	15.4%	5.5%	10.4%	18.5%	31.8%

5. CLOSING REMARKS

In this paper, we presented a method of deriving the aberrations sensitivity of shaped pupil coronagraphs. By employing bandlimited, non-binary representations of highly featured binary aperture functions, we were able to represent shaped pupil coronagraphs using an exit-pupil system model with reasonable grid sizes. From these models we found that the concentric ring mask coronagraphs have both a low sensitivity to low order aberrations as well as the ability to highly confine the energy that would otherwise of resulted in additional scattered over the entire science field. These characteristics are important features considering the scale of the TPF telescope concepts. With a large monolithic primary mirror and a highly separated off-axis secondary, it is easy to imagine how small dynamic low-order aberrations can persist. The relative insensitivity of the shaped pupil coronagraphs over image plane coronagraphs may make requirements on such instabilities more reasonable and ultimately reduce mission risk. It nevertheless remains to be seen how pupil plane masks play against the full virtues of image plane masks, which enable high contrast imaging at tighter IWAs at a higher efficiency. Telescope stability, imaging time, search space and wavefront sensing and control overhead costs are all factors that must be weighed together in optimizing the coronagraph architecture of TPF.

ACKNOWLEDGEMENTS

The research described in this paper was carried out at the Jet Propulsion Laboratory, California Institute of Technology, under a contract with the National Aeronautics and Space Administration.

REFERENCES

1. Trauger, J.T. et al, "Laboratory Technology validation for the Eclipse Coronagraphic Telescope," in preparation, Proc. SPIE Vol 5487, pp. 1-12 (2004).
2. Ford, V.G. et al, "Terrestrial Planet Finder Coronagraph," Proc. SPIE Vol 5170, pp. 1-12 (2003).
3. Kuchner, M.J., and Traub, W.A., "A Coronagraph with a band-limited mask for finding terrestrial Planets," ApJ 570, 2002.
4. Green, J.J., & Shaklan, S.B., "Optimizing coronagraph designs to minimize their contrast sensitivity to low-order optical aberrations," Proc. SPIE Vol. 5170, pp. 25-37 (2003).
5. Spergle, D., "A new pupil for detecting Extrasolar planets," astro-ph/0101142 (2000).
6. Kasdin, N.J., Vanderbei, R.J., Spergel, D.N, Littman, M.G., "Extrasolar planet finding via optimal apodized-pupil and shaped-pupil coronagraphs," ApJ Vol. 582, pp. 1147-1161 (2003).
7. Kasdin, N.J, Vanderbei, R.J., Littman, M.G, & Spergel, D.N., "Optimal asymmetric apodizations and shaped pupil for planet finding coronagraphy," submitted to Applied Optics (2004).
8. Vanderbei, R.J., Kasdin, N.J., Spergel, D.N., Kuchner, M., "New pupil masks for high-contrast imaging," Proc. SPIE vol. 5170, pp. 49-56 (2003).
9. Vanderbei, R.J., Spergel, D.N., & Kasdin, N.J., "Spiderweb Masks for High-Contrast Imaging," ApJ 590, pp. 593-603 (2003).
10. Vanderbei, R.J., Spergel, D.N., & Kasdin, N.J., "Circularly Symmetric Apodization via Star-shaped Masks," ApJ 599, pp. 686-694 (2003).
11. Vanderbei, R.J., Kasdin, N.J., & Spergel, D.N., "Rectangular-mask coronagraphs for high-contrast imaging," submitted to ApJ (2004).
12. Chanan G. and Troy, M., "Strehl ratio and modulation transfer function for segmented mirror telescopes as functions of segment phase error," Applied Optics, Vol 38 num 31, pp. 6642-47, November 1999.
13. Oppenheim A.V. and Schafer, R.W., *Digital Signal Processing*, Prentice Hall, New Jersey, 1989.
14. Gaskill, J.D., *Linear Systems, Fourier Transforms, and Optics*, John Wiley & Sons, New York, 1978.